Secondary radiation force between two closely spaced acoustic bubbles

Gabriel Regnault, Cyril Mauger, Philippe Blanc-Benon, Claude Inserra

Rapid Communications

Secondary radiation force between two closely spaced acoustic bubbles

Gabriel Regnault,[1,*] Cyril Mauger,[1] Philippe Blanc-Benon,[1] and Claude Inserra[2]
[1]*Univ Lyon, École Centrale de Lyon, INSA Lyon, CNRS, LMFA UMR 5509, F-69134 Écully, France*
[2]*Univ Lyon, Université Claude Bernard Lyon 1, Centre Léon Bérard, UMR 1032, LabTAU, France*

(Received 25 May 2020; accepted 10 September 2020; published xxxxxxxxxx)

Two acoustic bubbles may attract or repel due to the secondary radiation force acting on them. We use here a dual-frequency levitation chamber in order to trap two oscillating microbubbles at close, fixed distance, and to perform measurements of the interaction force. We successfully compare our measurements to a commonly used theoretical model that assumes linear spherical oscillations, and disregards attenuation and multiple scattering between bubbles. The deviation from the model arises when nonspherical surface oscillations are triggered, leading to an additional hydrodynamic force induced by second-order liquid flow.

DOI: 10.1103/PhysRevE.00.001100

Introduction. The acoustic radiation force is generated from the transfer of momentum flux from an imposed, external, oscillatory pressure field to a gas bubble. The force for which the incoming field comes from a driving ultrasound field is called primary radiation force. When coming from the radiated pressure of a nearby oscillating bubble, this force is called secondary radiation force. These radiation forces have been intensively used to control bubble motion in an ultrasound field, either to trap them by using their ability to resist to buoyancy and turbulence [1] or to propel gas bubbles for microswimming applications [2]. The secondary radiation force, named secondary Bjerknes force [3], can be either attractive or repulsive, depending on the bubbles characteristics. If the oscillations are in phase, the bubbles attract each other; if not, they repel each other [4]. While many theoretical studies extended the original theory to provide estimations of secondary radiation forces in a standing-wave field [5], by taking into account nonlinearity of bubble oscillations [6,7], and later multiple scattering between two interacting closely spaced bubbles [8], only few experimental results provided quantitative estimations of this force. The main experimental difficulty relies in the quantification of small amplitudes forces (typically in the range of nanonewtons) for a couple of closely spaced bubbles (interbubble distance less than ten times the bubble radius). For this reason many authors assess the interacting force from observation of their attractive motion when insonified. A pioneer study by Crum [5] measured the interaction force from the translational velocities of two attracting bubbles in a low-frequency (∼hertz) standing-wave field. This technique have been overhauled by other authors [9,10], for higher driving frequencies (∼kilohertz) and smaller bubbles (∼micrometers). Lanoy *et al.* [11] observed repulsive forces between a bubble pair, each of them located at the opposite side of the interface between water (freely moving bubble) and a yield-stress fluid (fixed bubble). The trajectory of the free bubble allows assessing secondary Bjerknes force, recovering attraction and repulsion features, and highlighting the importance of taking into account multiple scattering. For biomedical applications (megahertz frequencies for micrometer-diameter bubbles), Garbin *et al.* [12] measured the interaction forces between two free, optically trapped bubbles. Similarly to therapeutic ultrasound applications, short acoustic burst and coated bubbles were used, and secondary radiation forces were assessed from mutual attractive motion.

We report here an experimental method to assess simultaneously the bubble interface dynamics and the secondary Bjerknes force for free (nonattached), noncoated microbubbles at fixed interbubble distance. The influence of nonspherical bubble oscillations on the interaction force is also evidenced. Assessing interacting forces between stable oscillating bubbles is crucial as being a key mechanism in the self-organization of dispersed bubbles into structured clouds [13]. It is also worth noting that shape distortions between two interacting bubbles has only been observed in the case of strong coupling where one (or both) bubbles collapse and lead to breakup [14].

Experimental setup. We design a dual-frequency acoustic levitation chamber that enables the trapping of a bubble pair at a fixed distance while being acoustically excited. A schematic representation of the experimental setup is shown in Fig. 1(a). The experiments are conducted in an 8-cm-edge cubic tank filled with microfiltered and demineralized water (Carlo Erba, water for analysis). The microbubbles are generated at the tip of a thin capillary (inner diameter 20 μm) linked to a microfluidic pressure controller (Elveflow, OB1 MK3) supplied by an air compressor (Newport, ACWS). The capillary is located at the bottom of the water tank, generating an uprising, periodically spaced train of bubbles. The size of the microbubbles as well as the interbubble distance can be slightly influenced by tuning the input pressure using the controller. A bubble train of interdistance ∼1 mm and mean radius ∼100 μm is usually reached.

The bubble train is acoustically trapped within a standing-wave field generated by a high-frequency (HF) transducer (Sofranel IDMF018, 1 MHz nominal frequency) slightly immersed at the top side of the water tank. This HF field induces

*gabriel.regnault@insa-lyon.fr

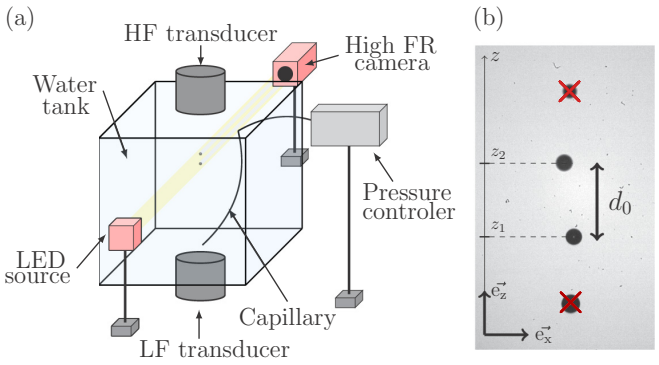

FIG. 1. (a) Schematic representation of the experimental setup used to assess secondary Bjerknes forces. (b) Photograph of a four-bubble train before bubble pair selection.

a primary radiation force that allows trapping the bubbles at successive pressure nodes, as the investigated bubbles (of radii ranging from 70 to 130 μm) are significantly greater than the resonant radius $R_{\text{res}}^{\text{HF}} \sim 3.3$ μm [13]. Due to the large contrast between the bubble size and the HF resonant radius, bubbles are trapped at rest in the wave field, meaning without experiencing radial oscillations. The interbubble distance is ~750 μm, corresponding to roughly six to ten bubble equilibrium radii, at rest. Figure 1(b) shows an example of a train of trapped bubbles that are, at this stage, not perfectly aligned vertically. Because the present study focuses on the interaction between a bubble pair, only two of them are kept. The selected pair of bubbles is such that the interbubble distance equals half a HF wavelength and their respective radii cover a broad range of radii distribution.

Once stabilized in the HF trapping field, the bubble oscillations are induced by a low-frequency (LF) Langevin transducer (RESON, 31 kHz nominal frequency) located at the bottom of the tank and emitting a 31.9 kHz continuous, sinusoidal waveform. We noticed no LF cavity resonance and negligible primary radiation force as the bubbles remain close to their trapping locations. The LF wavelength (~5 cm) is large compared to the radii of the bubbles and the interbubble distance. The bubble pair is therefore assumed to be driven at a uniform local pressure field. The dynamics of the bubble pair oscillations is captured with a CMOS camera (Vision Research V12.1) equipped with a 12× objective lens (Navitar). A backlight illumination is ensured by a continuous light-emitting diode (3 W LED). The recordings are performed with a frame size of 128 × 256 pixels, allowing a 130 kfps frame rate (opening time 1 μs). This frame rate allows quantifying the bubble interface dynamics (approximately four samples per acoustic period) in addition to the interbubble distance.

Characteristics of the HF trapping field. When a single bubble pair is trapped within the HF acoustic field, each bubble (of equilibrium radius $R_{0,i}$, $i = 1, 2$) experiences a force balance between the HF primary radiation force $\mathbf{F}_{B_1,i}$ and the buoyancy force $\mathbf{B}_i = -(\rho_l - \rho_g)V_i\mathbf{g}$, where ρ_l and ρ_g refer to the density of fluid and inner gas, respectively, V_i is the volume of the ith bubble, and $\mathbf{g} = -g\mathbf{e_z}$ is the geocentric gravitational acceleration. The periodically spaced, trapped, bubble train allows assuming a unidimensional plane-wave feature of the HF field $p_{\text{HF}}(z,t) = P_{\text{HF}} \sin(2\pi z/\lambda_{\text{HF}}) \sin(2\pi f_{\text{HF}} t)$, where P_{HF} is the acoustic pressure, λ_{HF} is the HF wavelength, and f_{HF} is the HF frequency. Thus the HF primary radiation force is written as

$$\mathbf{F}_{B_1} = \beta(R_{0,i}, f_{\text{HF}}, P_{\text{HF}}) \sin\left(4\pi \frac{z_i}{\lambda_{\text{HF}}}\right)\mathbf{e_z}, \qquad (1)$$

where β is a constant which depends on the bubble equilibrium radius $R_{0,i}$ and the acoustic field characteristics, and z_i is the location of the ith bubble center [5]. According to the bubble size contrast in comparison to the HF resonant radius $R_{0,i} \geqslant R_{\text{res}}^{\text{HF}}$, bubbles are acoustically trapped at successive pressure nodes $z_n^* = n\lambda_{\text{HF}}/2$, $n = 0, 1, \ldots$. Due to the buoyancy force, each bubble is in fact located above the theoretical pressure node of the HF standing-wave field (see Fig. 3).

Above the trapping pressure threshold $P_{\text{HF}}^{\text{th}}$ (for which $\|F_{B1,i}\| > \|B_i\|$), each bubble center location is experimentally measured during a step-by-step increase of the pressure P_{HF}. The vertical displacement of the bubble centers follows the spatial waveform of the primary radiation force given by Eq. (1), for which the locations z_i and radii $R_{0,i}$ are assessed. This allows estimating the trapping acoustic amplitude P_{HF}. Once the calibration curve of the trapping pressure is performed, the amplitude of the HF field is kept constant (typical value ~50 kPA) and results in an initial, interbubble vertical distance d_0.

Measurement of the secondary radiation force. Switching on the LF acoustic field induces bubble oscillations around their equilibrium radius $R_{0,i}$. The radiated acoustic pressure emitted by each bubble on the other is responsible for the generation of a local gradient of pressure leading to the secondary radiation force. Each bubble is therefore trapped at a

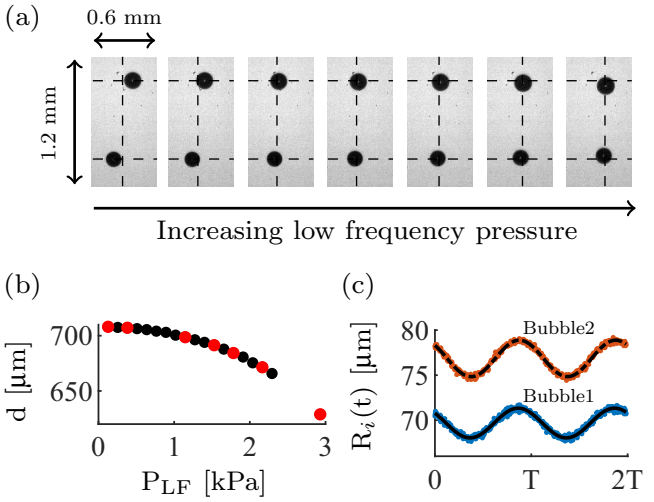

FIG. 2. (a) Extracts of two interacting bubbles for increasing LF field. (b) Evolution of the vertical interbubble distance as a function of the LF acoustic pressure P_{LF}. Each red dot corresponds to a snapshot photograph of (a). (c) Temporal evolution of the bubble radii, with respect to two acoustic periods, for the highest applied LF pressure.

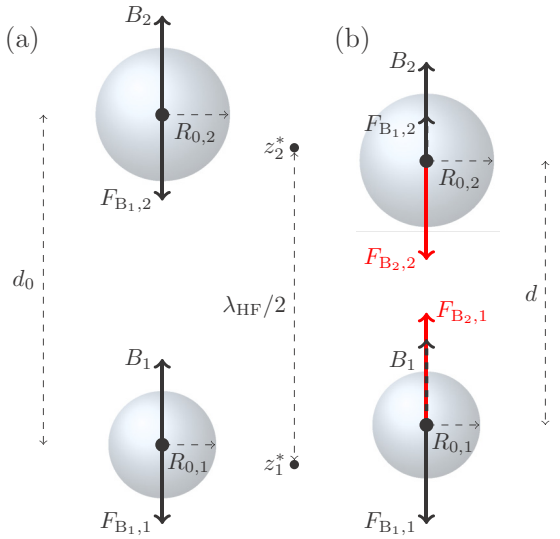

FIG. 3. (a) After acoustic trapping, each bubble experiences a force balance between buoyancy $\mathbf{B}_i$ and the primary HF radiation force $\mathbf{F}_{B_1,i}$. (b) A secondary interaction force $\mathbf{F}_{B_2,i}$ acts when the LF field is on, resulting in vertical attraction and repulsion of the bubble centers. z_n^* refers to the HF theoretical pressure nodes separated by half a wavelength, setting $n = 1$ for the lowest one (bubble 1).

new equilibrium location resulting from the force balance

$$\mathbf{F}_{B_1,i} + \mathbf{F}_{B_2,i} + \mathbf{B}_i = \mathbf{O}. \tag{2}$$

As shown in Fig. 2(a), the bubbles tend to align in the vertical direction. This evidences a predominant trapping force in the vertical direction compared to the one on the horizontal plane. As sketched in Fig. 3, the bubble centers may pass through the theoretical pressure nodes z_n^* if bubbles attract or even repel. When attraction occurs, bubbles will coalesce if one of the bubble centers location crosses half the distance to the next pressure antinode (i.e., where the primary Bjerknes force is maximum). This limits the achievable interbubble distance to $d_{\text{limit}} = \lambda_{HF}/4$, that is as small as 3.5 times the mean equilibrium radius for the largest investigated bubbles. The knowledge of the HF pressure P_{HF} allows fully determining the amplitude of the secondary radiation force $\mathbf{F}_{B_2,i}$, whose magnitude is theoretically identical for each bubble. All investigated bubble pairs are summarized in the $(R_{0,1}, R_{0,2})$ diagram in Fig. 4(a). Depending on the size of the bubble equilibrium radius relative to the LF resonant radius $R_{\text{res}}^{\text{LF}} \sim 103\mu$m, a bubble pair may experience attraction or repulsion. Cases of repulsive forces have been observed but are no longer analyzed as bubbles were rapidly repelled away from each other, out of the camera field and of its focal plane. All attractive bubble pairs exhibit purely spherical oscillations, except one couple [asterisk marker in Fig. 4(a)] for which one axisymmetric nonspherical mode was triggered. This case is discussed later.

The absolute value of the secondary radiation force for an attractive bubble pair $(R_{0,1}, R_{0,2}) = (97, 78)\,\mu$m trapped in a 78 kPa HF field is shown in Fig. 4(b). The forces measured on each bubble are nearly identical and exhibit the same trend for decreasing interbubble distance. The measured secondary radiation force is shown to be in remarkable agreement with

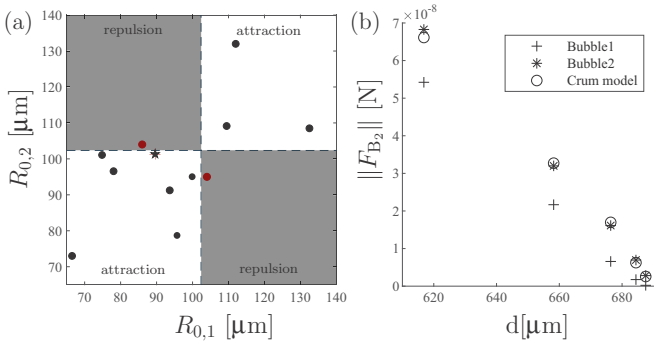

FIG. 4. (a) Bubble pairs radii distribution. Dashed lines correspond to the value of the LF resonant radius. (b) One series of experimentally assessed secondary Bjerknes forces.

the linearized model proposed by Crum [5]:

$$\mathbf{F}_{B_2,i} = -2\pi\rho\omega_{\text{LF}}^2 \frac{R_{0,1}^2\epsilon_1 R_{0,2}^2\epsilon_2}{d^2}\cos(\Delta\phi)\,\mathbf{u}_{r,i}, \tag{3}$$

where ω_{LF} is LF angular frequency, ϵ_i is the bubble expansion relative to the equilibrium radius, $\Delta\phi$ is the phase shift between bubble oscillations, and $\mathbf{u}_{r,i}$ is the unit vector along the axis passing through the centers of the bubble pair. To assess the coefficient ϵ_i, we notice that each bubble interface displays purely, almost linear, spherical oscillations [as those in Fig. 2(c)] ruled by $R_i(t) = R_{0,i}[1 + \epsilon_i\cos(\omega_{\text{LF}}t)]$. The Crum model assumes linear oscillations, distant bubbles, and disregards attenuation effects, such as the phase shift $\Delta\phi$ can only take the values 0 (bubble attraction) or π (bubble repulsion). At first sight, the secondary radiation forces cannot be compared for the whole experimental sets of bubble pair due to the variety of bubble equilibrium radii $R_{0,i}$ and trapping pressure P_{HF}. Therefore, a commensurable interaction force $\|F_{B_2}\|R_m/P_{HF}^2$ is investigated as a function of the normalized distance d/d_0 in Fig. 5. Here $R_m = (R_{0,1} + R_{0,2})/2$ is the mean bubble radius and $\|F_{B_2}\|$ is the mean value of the in-

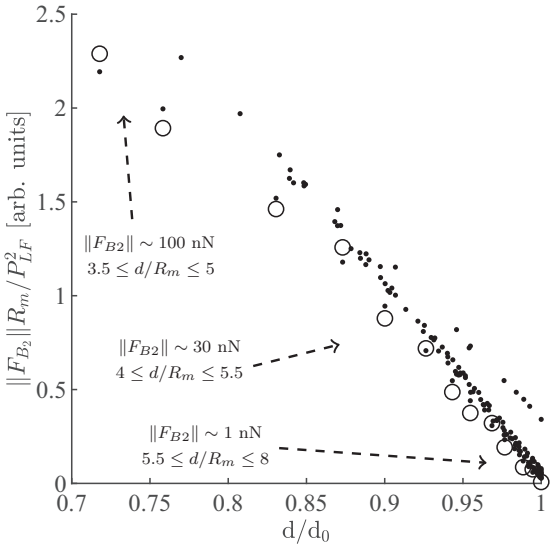

FIG. 5. Commensurable secondary Bjerknes forces $\|F_{B_2}\|R_m/P_{HF}^2$ for the whole set of attractive bubble pairs as a function of the normalized distance d/d_0.

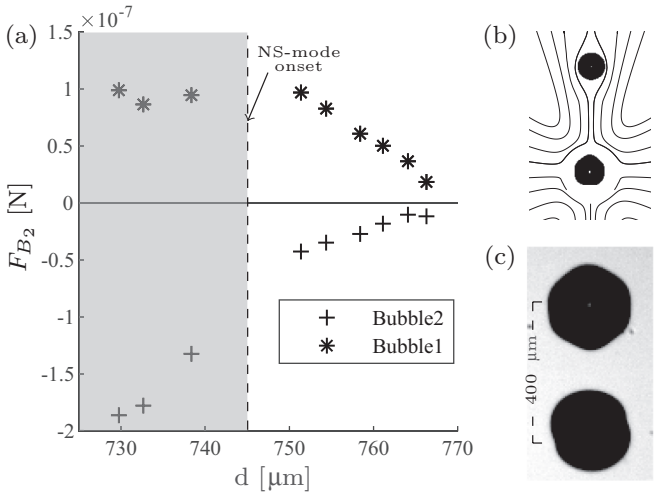

FIG. 6. (a) Secondary radiation force measured for each bubble as a function of the interbubble distance. The gray area indicates the onset of an axisymmetric shape mode on bubble 1. (b) Snapshot of the spherical and nonspherical interfaces of the bubble pair corresponding to (a). Expected streamlines are superimposed. (c) Extreme interbubble distances were observed when both bubbles exhibit nonspherical modes (bubble 1, undefined shape mode and bubble 2, axisymmetric sixth mode).

teraction force measured on each bubble. The factor R_m/P_{HF}^2 is found from the derivation of the interaction force between a bubble pair of similar sizes and close to their theoretical equilibrium location $z_i \sim z_i^*$. The agreement of the whole data sets along the linear relationship in Fig. 5 provides reliability in the proposed experimental method to assess the secondary Bjerknes force. In addition, the Crum model is validated for the whole set of investigated bubble pairs, even for the case $d/d_0 \sim 0.7$, meaning interbubble distances as close as ~3.5 bubble radius.

About bubble-induced hydrodynamic forces. It is known that a single free, spherically oscillating, microbubble does not induce second-order liquid flow due to the spherosymmetry of the resulting linearized acoustic velocity field [15]. Even if the theoretical investigation of the liquid flows generated by two oscillating bubbles have not yet been proposed, it may be suggested that symmetry breaking due to the presence of an in-vicinity oscillating bubble would lead to a supplementary hydrodynamic force. The results obtained for two spherically oscillating bubbles [Figs. 4(b) and 5] coupled to the agreement with the Crum model indicate that, if this hydrodynamic force exists, it is negligible in our experiment. However, significant vortical flows are produced when bubble oscillations include a translational [16] or nonspherical mode [17,18]. We recall that, for a bubble of equilibrium radius R_0 driven at the acoustic angular frequency ω, nonspherical instability arises above a particular pressure threshold [19]. This threshold has been reached for a bubble of equilibrium radius $R_{0,1} = 102\ \mu$m, while the other one ($R_{0,2} = 88\mu$m) remains spherical [Figs. 6(a) and 6(b)]. Below the onset of nonspherical oscillations, bubbles attract each other and the measured interaction force follows the same trend as previously observed. Once a surface mode is triggered, the secondary radiation force significantly deviates from its linear monotonous evolution. Recordings of the interface behavior of bubble 1 indicate the predominance of a subharmonic axisymmetric mode 5. Its bubble contour $r_1(\theta, t)$ can hence be written $r_1(\theta, t) = R_{0,1} + a_{0,1}\cos(\omega_{\mathrm{LF}}t) + a_{5,1}P_5(\cos\theta)\cos(\omega_{\mathrm{LF}}t/2)$, where we extract the modal coefficient $a_{0,1} \sim 4\mu$m, $a_{5,1} \sim 3\mu$m, and $P_5(\cos\theta)$ is the Legendre polynomial of degree $n = 5$.

Regarding that second-order streaming arises from the interaction of two modes oscillating at the same angular frequency ω [15], the only contribution of bubble 1 to the streaming flow is the self-interaction of the mode 5 with itself [20]. This self-interaction results in a crosslike pattern at large distance with lobelike vortices in the vicinity of the bubble interface. Figure 6(b) illustrates the expected pattern. Depending on the orientation of the nonspherical mode 5 in the $(\mathbf{e}_x, \mathbf{e}_z)$ plane, the branches of the crosslike pattern would present inward (leading to bubble 2 attraction) or outward (bubble 2 repelling) velocity vector field. The shift of the measured secondary radiation force from the linear relationship expected for purely spherical oscillations reveals that bubble 2 gets closer to bubble 1 due to the liquid flow. This suggests inward velocity field in the direction $2 \rightarrow 1$ on this cross branch. Injecting the value $a_{5,1}$ of the shape mode amplitude, the LF angular frequency, fluid properties, and the bubble equilibrium radius into the self-interacting shape mode-induced streaming [20] provides the order of magnitude of the radial velocity at the location of bubble 2, which is $v_{\mathrm{fl}} \sim 10\mu\mathrm{m\,s^{-1}}$. This results in a drag force applied on bubble 2 of the order of magnitude of ~ piconewtons. We recall that bubble 1 would experience a net force if it oscillates nonspherically with two nonzero adjacent modes $(a_{n,1}, a_{n+1,1})$ [21]. However, the modal analysis performed on bubble 1 only reveals odd nonspherical modes. No propulsive force is therefore expected. We experimentally estimate the net force experienced by each bubble to ~100 nN, obtained from Fig. 6(a) when computing the shift of secondary radiation force from the expected linear behavior. This suggests that the streaming pattern induced by two, closely spaced, oscillating bubbles may be significantly different from the one obtained in the single bubble case. Indeed multiple scattering of the linear acoustic field emitted by each bubble would lead to the broadening of mode interaction between the bubble pair, expected for extremely small interbubble distances, as small as $d \sim 400\ \mu$m, or equivalently $d/d_0 \sim 0.5$ [Fig. 6(c)], obtained when both bubbles oscillate nonspherically. The modeling of such multibubble-induced streaming field is still challenging.

Conclusions and perspectives. Measurements of secondary radiation force between trapped, free, interacting acoustic bubbles have been performed by means of a dual-frequency levitation chamber. In contrast to prior work where secondary Bjerknes force is exctracted using the bubble translational motion, here two closely spaced bubbles are trapped at fixed distance. Our measurements evidence the agreement with the Crum model for forces ranging over two orders of magnitude in the nanonewton scale, and allow investigating two interacting bubbles exhibiting nonspherical oscillations. Future work will aim at investigating the coupled nonspherical oscillations of a bubble pair, as well as the second-order liquid flows induced by two closely spaced bubbles, paving the way to the understanding of acoustofluidic interaction into a bubble cloud.

Acknowledgments. This work was supported by the LabEx CeLyA of the University of Lyon (ANR-10-LABX-0060/ANR-11-IDEX-0007). The authors also acknowledge A. A. Doinikov for helpful discussions.

[1] T. G. Leighton, A. J. Walton, and M. J. W. Pickworth, Eur. J. Phys. **11**, 47 (1990).
[2] N. Bertin, T. A. Spelman, O. Stephan, L. Gredy, M. Bouriau, E. Lauga, and P. Marmottant, Phys. Rev. Appl. **4**, 064012 (2015).
[3] V. F. K. Bjerknes, *Fields of force* (Columbia University Press , New York, 1906).
[4] M. Ida, Phys. Lett. A **297**, 210 (2002).
[5] L. A. Crum, J. Acoust. Soc. Am. **57**, 1363 (1975).
[6] A. Harkin, T. J. Kaper, and A. Nadim, J. Fluid Mech. **445**, 377 (2001).
[7] A. A. Doinikov, D. Bienaimé, S. R. Gonzalez-Avila, C.-D. Ohl, and P. Marmottant, Phys. Rev. E **99**, 053106 (2019).
[8] A. A. Doinikov and S. T. Zavtrak, Phys. Fluids **7**, 1923 (1995).
[9] J. Jiao, Y. He, S. E. Kentish, M. Ashokkumar, R. Manasseh, and J. Lee, Ultrasonics **58**, 35 (2015).
[10] T. Barbat, N. Ashgriz, and C.-S. Liu, J. Fluid Mech. **389**, 137 (1999).
[11] M. Lanoy, C. Derec, A. Tourin, and V. Leroy, Appl. Phys. Lett. **107**, 214101 (2015).
[12] V. Garbin, B. Dollet, M. Overvelde, D. Cojoc, E. Di Fabrizio, L. van Wijngaarden, A. Prosperetti, N. de Jong, D. Lohse, and M. Versluis, Phys. Fluids **21**, 092003 (2009).
[13] W. Lauterborn and T. Kurz, Rep. Prog. Phys. **73**, 106501 (2010).
[14] W. Lauterborn, T. Kurz, R. Mettin, and C. D. Ohl, Adv. Chem. Phys. **110**, 295 (1999).
[15] A. A. Doinikov, S. Cleve, G. Regnault, C. Mauger, and C. Inserra, Phys. Rev. E **100**, 033104 (2019).
[16] M. S. Longuet-Higgins, Proc. R. Soc. London, Ser. A **454**, 725 (1998).
[17] F. Mekki-Berrada, T. Combriat, P. Thibault, and P. Marmottant, J. Fluid Mech. **797**, 851 (2016).
[18] S. Cleve, M. Guédra, C. Mauger, C. Inserra, and P. Blanc-Benon, J. Fluid Mech. **875**, 597 (2019).
[19] M. P. Brenner, D. Lohse, and T. F. Dupont, Phys. Rev. Lett. **75**, 954 (1995).
[20] C. Inserra, G. Regnault, S. Cleve, C. Mauger, and A. A. Doinikov, Phys. Rev. E **101**, 013111 (2020).
[21] T. A. Spelman and E. Lauga, J. Eng. Math. **105**, 31 (2017).